Research Square

Preprints are preliminary reports that have not undergone peer review.
They should not be considered conclusive, used to inform clinical practice,
or referenced by the media as validated information.

Photoreceptor topography alters display and surround contributions to modeled receptor-weighted retinal stimulus during smartphone viewing

Salar Zaheryani
Kyung Hee University
Seung-Woo Lee
seungwoolee@khu.ac.kr

Kyung Hee University

Article

Keywords: smartphone display, surround luminance, photoreceptor topography, retinal stimulus, source attribution, α-opic weighting

Posted Date: November 19th, 2026

DOI: https://doi.org/10.21203/rs.3.rs-11450844/v1

License: This work is licensed under a Creative Commons Attribution 4.0 International License.
Read Full License

Additional Declarations: No competing interests reported.

Photoreceptor topography alters display and surround contributions to modeled receptor-weighted retinal stimulus during smartphone viewing

Salar Zaheryani, MD[1], Seung-Woo Lee, PhD[1*]

1. Convergence Display System Lab, Department of Information Display, Kyung Hee University, Seoul, South Korea

*: Corresponding Author: Seung-Woo Lee, PhD, Convergence Display System Lab, Department of Information Display, Kyung Hee University, Seoul, South Korea, seungwoolee@khu.ac.kr

Abstract

Smartphone displays viewed near fixation project onto cone-enriched central retina, whereas the surrounding visual field extends across rod-rich eccentric retina. We developed a source-resolved computational framework combining human photoreceptor topography, retinal-area mapping, α-opic spectral weighting, and pupil scaling to quantify display- and surround-derived contributions to receptor-weighted retinal stimulus. The display covered 4.60% of the modeled retinal area but contained only 3.89% of the rod population and 12.60% of the total-cone population. For the 40 $cd \cdot m^{-2}$ reference display at 10 $cd \cdot m^{-2}$ surround luminance, receptor topography reduced the rhodopic display-source fraction by 2.92 percentage points. Under total-cone weighting, it also increased the L-, M-, and S-cone-opic display-source fractions by 20.54–24.23 percentage points. This topography-dependent redistribution was greatest when display- and surround-derived contributions were comparable. Under near-dark viewing, the display dominated all receptor channels. The primary rod-depleted, total-cone-enriched topographic relationship remained robust across the tested sensitivity analyses. The framework provides a quantitative retinal-input basis for evaluating smartphone display conditions together with their surroundings.

Keywords: smartphone display; surround luminance; photoreceptor topography; retinal stimulus; source attribution; α-opic weighting

Introduction

A smartphone screen can occupy two markedly different visual contexts. In an illuminated room, it is embedded within a broadly illuminated scene; under near-dark viewing, the same display may become the dominant light source near fixation. Thus, display–surround contrast changes substantially as surround luminance decreases. Less clear, however, is whether the relative contributions of the display and its surroundings likewise change when retinal stimulation is considered across the photoreceptor populations sampling these regions.

This distinction is important because photoreceptors are not distributed uniformly across the retina. A smartphone viewed near fixation projects primarily onto the cone-rich central retina, whereas the surrounding visual field extends into rod-rich peripheral retina [1]. Moreover, the mapping between visual-field angle and retinal surface area is nonlinear, such that equal angular regions do not correspond to equal retinal areas [2]. Consequently, the same physical display–surround field may yield different relative contributions when stimulus is weighted according to retinal area or photoreceptor topography. Global descriptors such as display luminance, room illuminance, or mean-field luminance cannot, by themselves, capture this spatially and receptor-specific relationship.

The ambient context of near-device viewing is also experimentally relevant. Smartphone reading under low ambient illumination has been associated with greater visual discomfort than reading under illuminated conditions [3]. Lower ambient illumination during sustained near work has also been associated with larger immediate post-near refractive shifts [4]. Although these findings do not establish a retinal mechanism, they indicate that the surrounding light field can influence short-term visual responses while the near task remains similar. A quantitative description of retinal input may therefore provide better-defined conditions for subsequent physiological testing.

Previous work has addressed components of this problem separately. Spectral analyses of smartphone emission have characterized display spectra and wavelength-weighted visual and non-visual metrics without incorporating retinal spatial organization [5]. Visual-field luminance studies have related surrounding luminance and its spatial distribution to display preference and visual comfort [6-8]. Chu et al. invoked photoreceptor topography qualitatively to interpret radial comfort preferences [8]. However, measured receptor populations

have not been integrated quantitatively into display–surround source attribution. Studies of adaptation and the pupillary light reflex have further shown that central and peripheral stimulation can contribute differently to visual responses [9-11]. However, to our knowledge, these strands have not been integrated to quantify display- and surround-derived stimulus across measured human photoreceptor populations. The expected direction follows from established anatomy, because cones are concentrated centrally whereas rods predominate across much of the peripheral retina [1]. What remains unquantified is the magnitude of this topography-dependent redistribution of source attribution for a realistic smartphone field. Furthermore, its dependence on surround luminance, and its robustness to anatomical, spectral, and geometric uncertainty are yet to be established.

To address this gap, we developed a source-resolved, steady-state visual-field model. The framework incorporates α-opic spectral weighting [12], human rod and cone topography [1], nonlinear retinal-area mapping [2], pupil scaling [13], and reduced-eye retinal-stimulus geometry [14]. Using an otherwise identical uniform-density reference, the framework isolates the effect of measured receptor topography on display-versus-surround source attribution. Controlled lighting, spectral, polarity, geometric, and high-dynamic-range (HDR) analyses were then used to evaluate the framework across different display and environmental conditions and to assess the robustness of its predictions. The model characterizes retinal stimulus only; adaptation, neural responses, accommodation, refractive changes, and clinical outcomes remain experimentally testable questions. At 10 cd·m^{-2} surround luminance, measured photoreceptor topography increases cone-opic display-source attribution by more than 20 percentage points under total-cone weighting, while slightly reducing rhodopic attribution. The resulting framework provides a source-resolved quantitative basis for integrating retinal geometry, photoreceptor topography, and receptor-specific spectral weighting, while distinguishing topography-dependent population-level source attribution from region-averaged display–surround disparity.

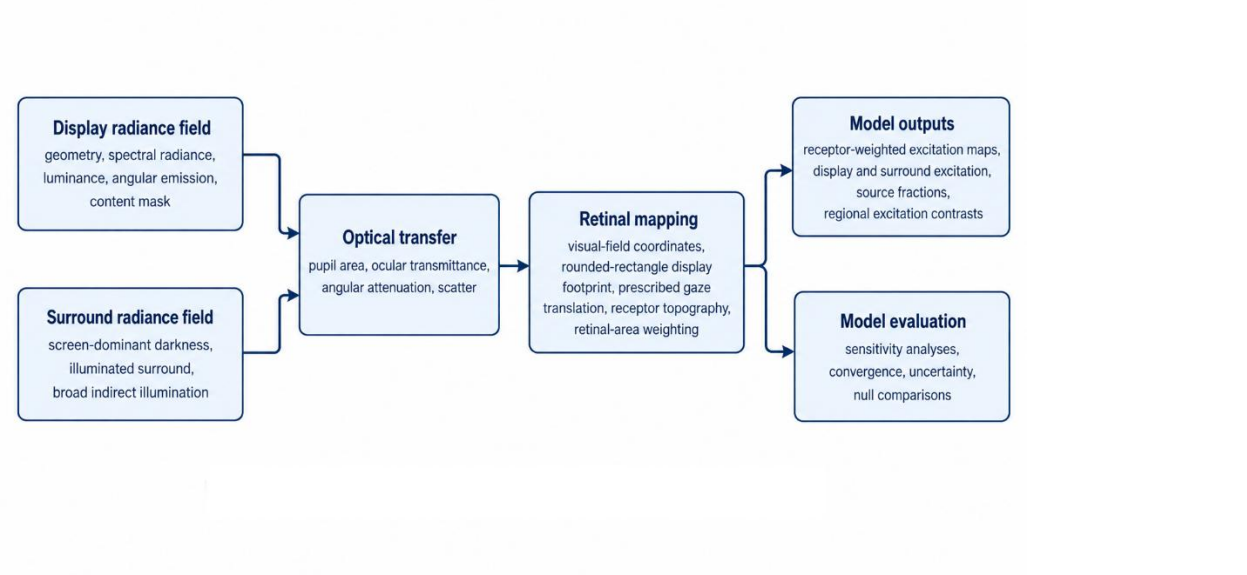


Figure 1. Computational architecture of the model. *Display and surround fields are transformed into receptor-weighted retinal stimulus through α-opic spectral weighting, pupil scaling, retinal-area mapping, and receptor topography. HDR surrounds were analyzed separately to characterize spatial heterogeneity.*

Results

Photoreceptor topography alters display–surround source attribution

Under the uniform-density reference, the display encompassed 4.60% of the modeled retinal area. However, when measured receptor topography was applied, it represented 3.89% of the modeled rod population and 12.60% of the total-cone population (Table 1, A). The display footprint was therefore relatively rod-depleted and total-cone-enriched compared with the uniform-density retinal-area reference.

This anatomical difference substantially altered source attribution at intermediate surround luminance. At 10 cd·m^{-2}, receptor topography reduced the rhodopic display-source fraction from 22.59% to 19.67%. Under total-cone anatomical weighting, the L-, M-, and S-cone-opic display-source fractions increased from 16.39%–23.20% to 36.92%–47.44% (Table 1, B; Fig. 2). The topography-dependent redistribution was smaller under near-dark viewing, where display-source fractions approached 100%, and at 50 cd·m^{-2}, where the surround dominated. Thus, the topography-dependent redistribution was greatest when display- and surround-derived contributions were more closely balanced.

The same separation was reflected in the model-defined crossover luminance, which occurred at 2.45 cd·m^{-2} for the rhodopic channel and 5.85–9.02 cd·m^{-2} for the cone-opic channels. Because crossover luminance depends on the spatial integration domain, the sensitivity of the rhodopic crossover estimate to analysis radius is reported in Supplementary Table S2(A).

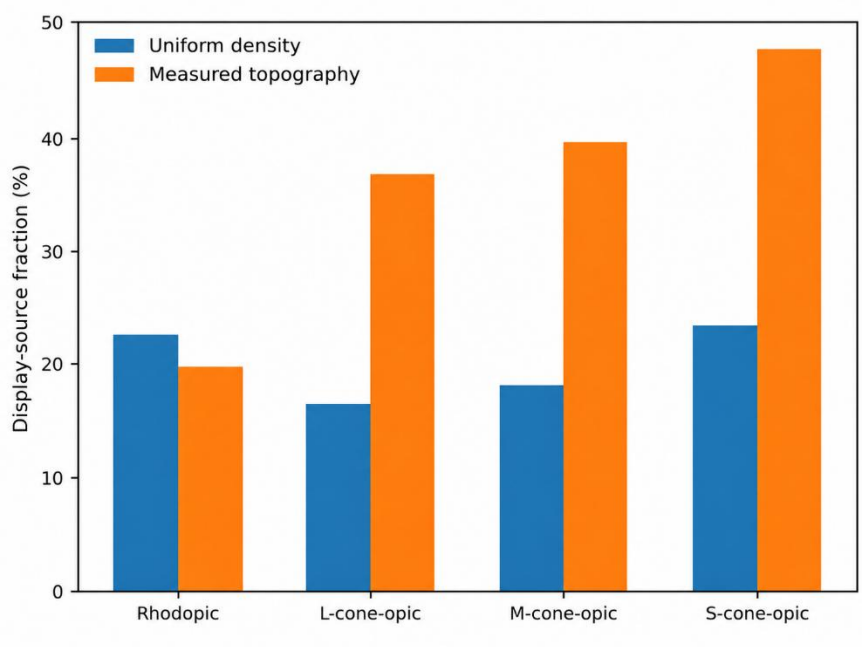


Figure 1. Effect of photoreceptor topography on display-source fraction. *Display-source fractions at 10 cd·m^{-2} surround luminance are compared between the uniform-density reference and measured receptor topography. Applying receptor topography reduced the rhodopic display-source fraction by 2.92 percentage points and increased L-, M-, and S-cone-opic display-source fractions by 20.54–24.23 percentage points.*

Table 1 Anatomical display-footprint overlap and effects of photoreceptor topography on display-source attribution.

(A) Anatomical overlap of the display footprint	
Anatomical weighting	**Display overlap (%)**
Uniform-density retinal-area reference	4.60%
Rod topography	3.89%
Total-cone topography	12.60%

(B) Effect of topography on display-source fraction			
Spectral Channel	**Display-source fraction, uniform density (%)**	**Display-source fraction, measured topography (%)**	**Topography-dependent change (percentage points)**
Rhodopic	22.59	19.67	−2.92
L-cone-opic	16.39	36.92	+20.54
M-cone-opic	18.10	39.76	+21.66
S-cone-opic	23.20	47.44	+24.23

Note: *(A) The uniform-density value represents the fraction of modeled retinal area occupied by the display, whereas rod and total-cone values represent the fractions of their respective modeled populations within the display footprint. (B) Values correspond to a 40 cd·m⁻² display and 10 cd·m⁻² surround. Rhodopic calculations use rod topography, whereas all three cone-opic channels use the same measured total-cone topography in the primary analysis. Cone-subtype-specific spatial distributions were evaluated separately in sensitivity analyses. Changes in percentage points (pp) are calculated from unrounded results.*

Surround luminance shifts display-source fraction and regional retinal illuminance

Under near-dark viewing (0.01 cd·m⁻²), the display-source fraction was 99.59% for the rhodopic channel and 99.83–99.89% across the cone-opic channels. Increasing surround luminance to 10 cd·m⁻² reduced the display-source fraction to 19.67% for the rhodopic channel and 36.92–47.44% across the cone-opic channels. At 50 cd·m⁻², it decreased further to 4.67% and 10.48–15.29%, respectively (Fig. 3A). Thus, the display dominated all receptor channels under near-dark viewing, whereas increasing surround luminance progressively shifted source attribution toward the surround. Under illuminated conditions, the display-source fraction remained higher for the cone-opic channels than for the rhodopic channel.

Near-dark viewing also produced the greatest regional disparity between the display core and extra-display surround (Fig. 3B). Regional disparity (Δα), defined in the Methods, ranged from 3.60 to 3.78 $\log_{10}$ units across the rhodopic and cone-opic channels at 0.01 cd·m⁻². At 10 cd·m⁻², Δα decreased to 0.61–0.79 $\log_{10}$ units, corresponding to a reduction of approximately 2.99 $\log_{10}$ units relative to near-dark viewing. At 50 cd·m⁻², Δα ranged from −0.09 to 0.10 $\log_{10}$ units, corresponding to a reduction of 3.69 $\log_{10}$ units. Consistent with this convergence, the idealized source-specific photopic and scotopic retinal-illuminance estimates decreased for

the display and increased for the surround as surround luminance increased (Table 2). Photopic and scotopic retinal-illuminance estimates showed the same overall pattern.

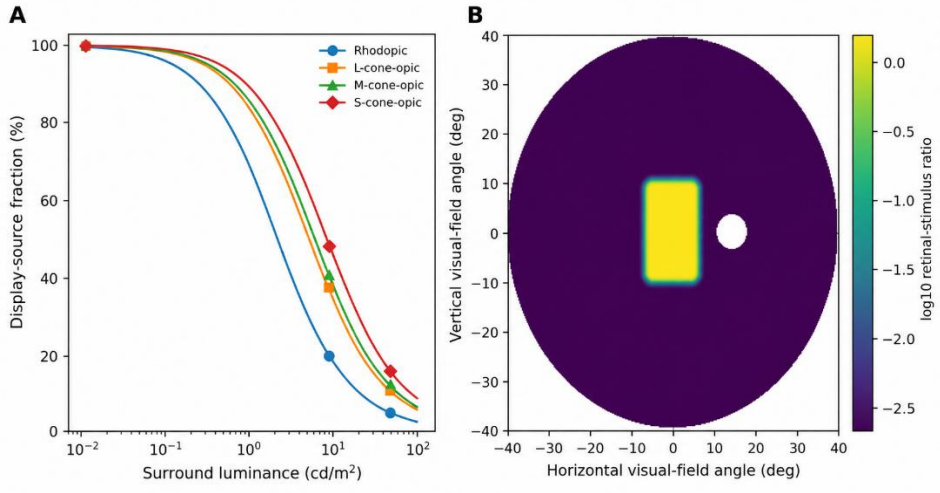


Figure 3. Surround luminance alters display-source fraction and regional retinal stimulus. *(A) Model-predicted display-source fractions under measured receptor topography as a function of uniform surround luminance for the rhodopic and L-, M-, and S-cone-opic channels. Curves were calculated from the source-attribution model; markers indicate the 0.01, 10, and 50 cd·m⁻² reference conditions. (B) Spatial distribution of the rhodopic $\log_{10}$ retinal-stimulus ratio under near-dark viewing (0.01 cd·m⁻²) relative to the 10 cd·m⁻² surround condition. Near-dark viewing produced greater modeled stimulus within the display footprint and markedly lower stimulus in the extra-display surround. The white region denotes the excluded optic-disc area.*

Table 2 Source-specific photopic and scotopic retinal illuminance across surround-luminance conditions.

Surround luminance (cd·m^{-2})	Display source, photopic T_d	Surround source, photopic T_d	Display source, scotopic T_d	Surround source, scotopic T_d
0.01	640.53	0.16	1667.93	0.28
10	395.75	98.94	1030.52	170.31
50	275.32	344.15	716.93	592.41

Note: *Values represent idealized display- and surround-source retinal illuminance calculated from nominal source luminances and condition-specific pupil area. Scotopic values additionally account for source-specific scotopic-to-photopic ratios. These estimates do not incorporate the spatial display-mask transition and are distinct from the retinal-area-weighted regional α-opic stimulus means used to calculate Δα. Td, troland.*

Effects of controlled display and surround conditions

Increasing surround luminance consistently reduced regional disparity, whereas lowering display luminance primarily reduced stimulus within the display core. For the 40 cd·m^{-2} reference display, surround luminance was increased from the 0.01 cd·m^{-2} near-dark reference to the low-level diffuse-surround conditions (Controlled display and surround analyses in Methods). This transition reduced regional disparity across the rhodopic and cone-opic channels by 2.20 $\log_{10}$ units at 1.6 cd·m^{-2} and by 2.51 $\log_{10}$ units at 3.3 cd·m^{-2}. Under these spatially uniform conditions, the change in regional disparity was not materially dependent on receptor topography.

As expected from the region-averaged definition of Δα, the phase-averaged negative-polarity condition with a 25% average picture level (APL) yielded a result similar to that of a uniformly dimmed display with the same mean luminance. The difference in Δα was less than 0.001 $\log_{10}$ units across all receptor channels. This comparison therefore serves primarily as a control demonstrating that Δα is insensitive to within-display luminance arrangement when mean display luminance is matched. Changing the display white point to 5000 K altered receptor-specific stimulus magnitude, while the corresponding change in regional disparity ranged from −0.103 to +0.001 $\log_{10}$ units relative to the D65-like reference under the tested conditions (Table 3).

Table 3 Effects of controlled display and surround conditions on modeled regional disparity.

Controlled condition	Comparison	Regional-disparity result
Low-level diffuse surround	Near-dark, 0.01 → 1.6–3.3 cd·m⁻² surround, at fixed 40 cd·m⁻² display	Δα reduced by 2.20 $\log_{10}$ units at 1.6 cd·m⁻² and 2.51 $\log_{10}$ units at 3.3 cd·m⁻²
Uniform display dimming	40 → 10 cd·m⁻² at fixed 10 cd·m⁻² surround	Δα reduced by approximately 0.60 $\log_{10}$ units across channels
25%-APL negative polarity	Compared with a uniform 10 cd·m⁻² display at matched mean luminance; 10 cd·m⁻² surround	Absolute difference in phase-averaged Δα was less than 0.001 $\log_{10}$ units across channels.
5000-K display	Compared with D65-like spectrum; 40 cd·m⁻² display and 10 cd·m⁻² surround	Δα difference (5000 K minus D65-like) ranged from −0.103 to +0.001 $\log_{10}$ units across channels.

Robustness of the topographic findings

The principal topographic relationship was preserved across the tested anatomical, spectral, geometric, and viewing-condition variations. Across the constrained anatomical perturbations, the display remained rod-depleted and total-cone-enriched relative to the uniform-density reference. The same pattern was retained across all 300 jointly sampled combinations of display luminance, viewing distance, and near-dark surround luminance. Specifically, the display-overlap ratio remained below 1 for rods (0.655–0.951) and above 1 for total cones (2.227–3.785).

Cone-subtype sensitivity analyses showed greater variation in channel-specific estimates than the primary rod-versus-total-cone comparison. In particular, alternative wide-field L/M spatial weighting shifted L- and M-cone-opic display-source fractions by as much as 46.97 percentage points in the most extreme tested case. Despite this subtype-level sensitivity, the broader rod-depleted, total-cone-enriched topographic relationship was preserved. Spectral substitutions likewise shifted receptor-specific display-source fractions while preserving the broader separation between rhodopic and cone-opic source attribution. Fixed-pupil control confirmed that condition-dependent pupil scaling changed absolute retinal-stimulus magnitude but not the normalized display-source fraction. Grid-spacing and display-corner-radius variations produced only small changes in the primary findings, whereas the domain-dependent crossover luminance varied more substantially with analysis radius. Detailed sensitivity and numerical results are provided in the Supplementary Information.

Spatially heterogeneous HDR surrounds

Across the 400 scene–gaze conditions, mean extra-display luminance had a median of 25.76 cd·m⁻² (10th–90th percentile, 3.88–93.38 cd·m⁻²). Across the sampled scene–gaze conditions, the median signed difference in display-source fraction between HDR surrounds and their mean-matched uniform counterparts was close to zero. At 40 cd·m⁻² display luminance, the median HDR-minus-uniform difference was +0.023 percentage points for the rhodopic channel and approximately −0.003 percentage points for the cone-opic channels. Individual scene–gaze conditions showed greater variation, with differences ranging from −1.39 to +1.74 percentage points for the rhodopic channel and from −8.64 to +3.60 percentage points across the cone-opic channels.

At 10 cd·m⁻² display luminance, median differences likewise remained near zero. Differences ranged from −0.57 to +1.25 percentage points for the rhodopic channel and from −7.15 to +2.35 percentage points across the cone-opic channels (Supplementary Table S3). Thus, the median signed effect of spatial heterogeneity was small in the sampled indoor scenes, although individual scene–gaze combinations produced larger deviations from the mean-matched uniform approximation.

Discussion

The present model shows that photoreceptor topography alters how a centrally viewed smartphone display and its surrounding visual field contribute to receptor-weighted retinal stimulus. Although the display occupied 4.60% of the retinal-area reference, it represented only 3.89% of the modeled rod population and 12.60% of the total-cone population. This difference substantially altered source attribution when display and surround contributions were of comparable magnitude. At 10 cd·m⁻² surround luminance, measured receptor topography reduced the rhodopic display-source fraction by 2.92 percentage points relative to uniform-density reference. Conversely, it increased the L-, M-, and S-cone-opic display-source fractions by 20.54–24.23 percentage points. The main result is therefore not simply that a smartphone display produces greater retinal stimulus in the central field than the surrounding field. Rather, the same physical display–surround field is apportioned differently when stimulus is integrated according to the markedly different spatial distributions of rods and cones.

This distinction helps define the specific contribution of receptor topography within the model. Display geometry, luminance, spectral composition, and retinal projection establish the spatial stimulus pattern. Receptor topography then determines how strongly different regions of that pattern contribute when integrated across a receptor population. Topography therefore does not create the local display–surround contrast; rather, it changes the population weighting assigned to the central display and the surrounding field. This comparison with an otherwise identical uniform-density reference is central to the present analysis. By holding retinal-area mapping, geometry, spectra, and pupil treatment constant, we isolate the specific effects of varying receptor distribution. Chawla and Samei considered adaptation changes associated with gaze transitions between a bright display and darker surrounding surfaces [9]. Gloriani et al. showed that adaptation varies with background luminance, field size, and retinal eccentricity [10]. Sonntag et al. further demonstrated distinct contributions of central and peripheral stimulation to cone- and rod-specific pupillary responses [11]. The present framework addresses a complementary question by quantifying display-versus-surround source attribution across measured human photoreceptor topography, without modeling adaptation or downstream physiological responses.

The population-integrated display-source fraction may also provide a basis for investigating physiological responses that combine inputs across different retinal regions. For example, the pupillary light reflex involves distinct contributions from central and peripheral rod- and cone-mediated stimulation [11]. However, these contributions are not necessarily proportional to photoreceptor population size or modeled stimulus magnitude. The present source fractions therefore characterize receptor-weighted retinal input rather than predicting pupillary or other downstream physiological responses.

Near-dark viewing also produced the greatest regional disparity between the display core and the extra-display surround. As surround luminance decreases, the display can therefore remain a strong central source while much of the extra-display surround receives substantially less stimulus. This regional disparity reflects the display-to-surround stimulus relationship rather than receptor topography, whereas receptor topography separately determines how display- and surround-derived light contribute to population-integrated rod- and cone-weighted retinal stimulus. This modeled difference provides a quantitative retinal-input context for the ambient-dependent visual and short-term refractive responses introduced earlier [3,4], without implying that

regional disparity causes those responses. Rather, it defines a measurable stimulus condition that can be evaluated directly in subsequent physiological experiments.

The controlled analyses further showed that modest increases in diffuse-surround luminance substantially reduced regional disparity. This effect primarily reflected the change in the display-to-surround stimulus relationship rather than receptor topography, which instead influenced the population-integrated display-source fraction. This range was selected as a representative low-level illuminated surround and should not be interpreted as a direct conversion of the eye-level illuminance measurements reported by Miller and Kinzey [15]. The relevant physical quantity in the model, however, is the luminance of the visual surround at the observer. The direction of this modeled effect is broadly consistent with findings from Antona et al. [3], who reported greater smartphone-related symptoms during reading in darkness. It is also consistent with Na and Suk [16], who found lower preferred display luminance during initial smartphone viewing under very low illuminance. Xu et al. [6] further reported an expanded visual-comfort range when controlled ambient lighting was introduced around a visual display terminal (VDT) under low-light conditions. Wang et al. [7] showed that the spatial distribution of ambient luminance affects preferred smartphone display luminance and visual comfort. Chu et al. [8] further investigated preferred spatial luminance distributions for visual comfort and reported that peripheral attenuation varied with visual-field eccentricity and central luminance, becoming less pronounced at lower central luminance. Because their experimental profiles were constrained to be non-increasing toward the periphery, these findings characterize the preferred magnitude of attenuation rather than independently establishing its direction. Together, these findings suggest that spatial luminance distribution, rather than mean luminance alone, may be relevant. This consideration also applies when characterizing environmental lighting in relation to modeled retinal-stimulus disparity and when designing future experiments examining pupillary, accommodative, or subjective responses.

The display manipulations also illustrate a boundary of the regional-disparity metric. At matched mean display luminance, the negative-polarity and uniformly dimmed conditions yielded similar Δα values, as expected from its region-averaged definition. Because Δα averages α-opic stimulus within the display core, it is not designed to capture polarity-dependent spatial structure within that region. Evaluating such effects would require an additional within-display spatial metric. This limitation is relevant because dark mode is not a single photometric condition. Dark-mode implementations can differ in text–background luminance contrast and in the luminance and color composition of interface elements [17,18]. The resulting receptor-specific retinal stimulus can also depend on the spectral characteristics of the underlying display technology [19]. Characterizing these physical properties rather than the interface label itself would allow different display modes to be compared in terms of the receptor-specific retinal stimulus they produce. The present analysis therefore demonstrates the behavior and scope of the current metric rather than defining an optimized dark-mode configuration.

This spectral dependence is also relevant to interventions that reduce short-wavelength light, although evidence for symptomatic benefit from blue-light filtering remains inconsistent. Some studies have reported changes in critical flicker fusion or selected symptoms with greater short-wavelength attenuation [20,21]. Conversely, subsequent controlled studies have found little or no benefit for digital eye-strain symptoms [22-24]. The present model addresses a different question: it quantifies how spectral modification changes receptor-specific retinal input and source attribution rather than predicting visual comfort or symptom relief. The distinction between intervention types is also important for source-resolved analysis. Spectacle filters modify both display- and ambient-derived spectra reaching the eye, whereas display-based night-shift or warmer-white modes selectively modify the display source. The framework can therefore distinguish spectral modifications applied to the display from those affecting the entire visual field.

The HDR analysis extended the framework from spatially uniform surrounds to calibrated indoor scenes. Across 400 scene–gaze combinations, the median HDR-minus-uniform difference in display-source fraction was close to zero. At 40 $cd \cdot m^{-2}$ display luminance, individual HDR conditions differed by −1.39 to +1.74 percentage points for the rhodopic channel and −8.64 to +3.60 percentage points across the cone-opic

channels. Thus, mean surround luminance captured much of the source-attribution behavior in these scenes. However, remaining deviations indicate that spatial luminance distribution can become relevant when different parts of the environment project onto retinal regions with different receptor weighting.

Condition-dependent pupil diameter changed absolute retinal-stimulus magnitude but not normalized display-source attribution because pupil area scaled display- and surround-derived contributions equally within each condition. The fixed-pupil control confirms this property of the present model, but it should not be interpreted as evidence that pupil changes are physiologically unimportant. Ocular aberrations and retinal image quality vary across the visual field, effects that are not represented by the present scalar pupil-area treatment [25]. The current framework represents pupil diameter only as a scalar collecting-area term. Therefore, it does not model pupil-entry directionality, including the Stiles–Crawford effect, or spatially varying optical quality across the visual field. In our implementation, the Watson–Yellott model [13] was supplied with a solid-angle-weighted mean adapting luminance. Hence, it did not represent potentially different contributions of central and peripheral stimulation to the pupil response [11]. The equivalent 80° adapting field was selected to correspond to the modeled 40° visual-field radius rather than to reproduce a specific experimental adaptation field. Accordingly, the resulting pupil diameters and troland values should be regarded as model-based steady-state estimates rather than precise physiological predictions of pupil behavior.

The pronounced spatial imbalance predicted during near-dark viewing nevertheless provides a candidate retinal-input condition for experimental investigation. As a hypothesis-generating analogy, studies of spatially nonuniform retinal signals have shown that peripheral hyperopic defocus can alter central refractive development in experimental animals [26]. Human studies, however, have reported more mixed associations between peripheral refraction and subsequent myopia [27, 28]. The disparity modeled here is not optical defocus and should not be considered an equivalent mechanism. It may nevertheless define a different spatial retinal-input context in which accommodative and other visual signals are generated during sustained near work. Near work-induced transient myopia provides one possible short-term experimental endpoint [29], alongside accommodation, pupil dynamics, visual symptoms, and fixation behavior. Testing these possibilities would require controlled human experiments in which display and surrounding luminance are measured at the observer’s position and manipulated independently.

The main anatomical relationship remained stable across the tested sensitivity analyses. Across constrained perturbations of the rod and total-cone distributions reported by Curcio et al. [1], the display remained rod-depleted and total-cone-enriched relative to the uniform-density reference. The same relationship was preserved across all 300 jointly sampled combinations of display luminance, viewing distance, and near-dark surround luminance. Cone-subtype sensitivity analyses altered some channel-specific estimates but did not overturn this broader separation. Direct S-cone measurements from Curcio et al. [30] supported the central domain containing the display, whereas peripheral S-cone assumptions were bounded using the anatomical observations of Ahnelt et al. [31]. Spatial variation in L/M weighting was examined using the wide-field functional measurements of Kuchenbecker et al. [32], rather than assuming a universal anatomical L:M distribution. These analyses support the rod-versus-total-cone topographic relationship as the most robust anatomical result, whereas subtype-specific estimates remain more dependent on the available anatomical and functional evidence.

Several additional limitations define the scope of the predictions. The receptor maps represent composite reference anatomy rather than an individual observer. Consequently, interindividual differences in receptor density, cone-subtype composition, retinal geometry, ocular media, and macular pigment could alter receptor-specific estimates. The controlled analyses assume centered viewing and simplified surrounds, whereas the HDR scenes provide calibrated examples rather than measurements of an observer's actual viewing environment. The reference display geometry was derived from manufacturer-reported specifications [33] for the handset examined by Yeo et al. [34], while the spectral basis was derived from published screen-emission measurements [34]. The digitized RGB spectra were treated as relative spectral-shape templates rather than

calibrated spectral-radiance measurements. Gaze and head motion, temporal adaptation, screen reflectance, viewing-angle-dependent emission, and condition-dependent fixational eye movements were not simulated.

The model also does not simulate ocular straylight or glare-related retinal-image spread. A physiologically grounded extension would require a validated wide-angle straylight formulation, such as the CIE/Vos–van den Berg disability-glare model, rather than an arbitrary Gaussian blur [35]. More generally, the present calculations stop at receptor-weighted retinal input and do not include photopigment adaptation, retinal gain control, post-receptor processing, perceived brightness, visual discomfort, accommodation, or refractive responses. The modeled regional disparity should therefore not be interpreted as a neural contrast metric or as a direct measure of visual strain.

The present framework provides a source-resolved means of moving beyond global descriptors such as screen luminance or room illuminance when characterizing smartphone viewing. By integrating visual-field geometry, photoreceptor topography, and receptor-specific spectral weighting, it enables display and surround conditions to be compared in terms of population-weighted retinal input. This is relevant to real-world night-time use, for which low eye-level illuminance during smartphone viewing has been reported [15]. The resulting stimulus conditions can provide a quantitative basis for subsequent human experiments examining pupil, accommodative, refractive, or subjective responses, while their physiological significance remains to be determined empirically.

Methods

Study design and scope

We developed a steady-state computational model using published anatomical, spectral, colorimetric, pupil, and reduced-eye data. The model calculated source-resolved, receptor-weighted retinal stimulus from the smartphone display and its surround. Measured photoreceptor topography was compared with an otherwise identical uniform-density reference to isolate the effect of receptor distribution on display-versus-surround source attribution. The framework was also applied to controlled display–surround conditions and spatially heterogeneous HDR scenes. The model characterized retinal input and did not simulate temporal adaptation, retinal neural responses, accommodation, or refractive changes.

Physical stimulus and viewing conditions

The commercial active-matrix organic light-emitting diode (AMOLED) handset examined by Yeo et al. [34] was used as the reference device. Display geometry was derived from its manufacturer-reported 5.1-inch, 2560 × 1440 specification [33], yielding a portrait-oriented active area of approximately 63.51 × 112.90 mm. At a viewing distance of 330 mm, the display subtended approximately 10.99° × 19.41° and was modeled at 40 $cd \cdot m^{-2}$. Three spatially uniform surrounds were examined at 0.01, 10, and 50 $cd \cdot m^{-2}$, representing near-dark, illuminated, and bright viewing conditions, respectively. These conditions varied surround luminance while holding display geometry, luminance, and spectral inputs constant. Spatially heterogeneous surrounds were examined separately using calibrated HDR scenes. The model was parameterized to accommodate other device dimensions, viewing distances, luminances, and spectra without changing its underlying structure. The complete reference conditions and sensitivity-analysis ranges are provided in Supplementary Table S1.

Spectral inputs and display-spectrum construction

Spectral calculations were performed from 380 to 780 nm at 1-nm intervals. Normalized red-, green-, and blue-screen emission spectra digitized from Yeo et al. [34] were used as the reference AMOLED spectral basis. A

measured AMOLED spectrum digitized from Fig. 3(c) of Oh et al. [5] was evaluated separately as a display-spectrum sensitivity case. The reference ambient spectrum was the CIE LED-B3 standardized LED spectral distribution, with CIE LED-B1 and LED-B5 evaluated separately as ambient-spectrum sensitivity cases [36]. CIE 1931 2° color-matching functions were used for colorimetric calculations [37]. Similarly, the CIE S 026 energy-based action spectra were used to calculate rhodopic and L-, M-, and S-cone-opic quantities [12].

For each source spectrum $S_j(\lambda)$ and receptor channel α, the α-opic efficacy of luminous radiation was calculated according to CIE S 026 [12]:

$$K_{\alpha,v}^{(j)} = \frac{\int S_j(\lambda) s_\alpha(\lambda) d\lambda}{K_m \int S_j(\lambda) V(\lambda) d\lambda}, \quad (1)$$

where $s_\alpha(\lambda)$ is the CIE S 026 energy-based action spectrum for α, $V(\lambda)$ is the photopic luminous-efficiency function, and K_m = 683 lm W^{-1}. Because the spectra were represented as relative spectral distributions, their arbitrary normalization canceled in the ratio. At each visual-field location x, the photopic luminance of each source was converted to α-opic radiance as

$$L_{\alpha,j}(x) = L_{v,j}(x) K_{\alpha,v}^{(j)}, \quad (2)$$

where $L_{v,j}(x)$ is the photopic luminance of the display or ambient source at location x.

Display spectra were constructed by linearly combining the AMOLED primary spectra to achieve the specified white points and were subsequently scaled to the assigned display luminance. The reference display used a D65-like white point, whereas a 5000-K white point was examined as a spectrally modified display condition. The AMOLED primary spectral templates and the synthesized D65-like and 5000-K display spectra are shown in Supplementary Fig. S1. No additional ocular-media transmission filter was applied beyond the receptor spectral weighting represented by the CIE S 026 action spectra. Additional details of spectral construction and sensitivity analyses are provided in Supplementary Methods.

Receptor topography and retinal coordinates

Human rod and total-cone topographies were derived from the Curcio datasets [1]. Retinal coordinates were converted to visual-field angles using the Drasdo–Fowler relationship [2], with retinal-image inversion applied. The optic-disc region was excluded using the Curcio location data and the mean disc dimensions reported by Quigley et al. [38]. Population weighting incorporated the retinal surface area represented by each visual-field location; thus, equal angular grid cells were not treated as equal retinal areas. For grid location i,

$W_{\alpha,i} = D_{\alpha,i} A_i$, (3) where $D_{\alpha,i}$ is the receptor-density weighting for channel α, and A_i is the retinal area represented by grid location i.

For the primary cone-opic calculations, total-cone topography provided the whole-field anatomical basis; cone-subtype-specific spatial distributions were evaluated separately in sensitivity analyses. Direct human S-cone measurements from Curcio et al. [30] extended to 14.36° after application of the same retinal mapping. The rectangular bounding geometry of the modeled display reached approximately 11.15° eccentricity in visual-angle coordinates, and the display footprint with a 1° corner radius was contained within this bound. The entire display footprint therefore lay within the directly measured S-cone domain. Within this domain, combined L+M cone density was calculated as total-cone density minus S-cone density. Beyond the measured S-cone domain, peripheral S-cone fractions were evaluated as bounded sensitivity cases based on Ahnelt et al. [31]. Because no universal anatomical L:M distribution is available, spatial variation in L/M weighting was examined using the wide-field functional weighting [32], rather than represented as a measured density map.

Melanopic weighting was not included because the framework was based on rod and cone photoreceptor topography rather than the distinct anatomical distribution of melanopsin-containing intrinsically photosensitive retinal ganglion cells.

The 40° reference radius was selected to capture the visual-field context surrounding a centrally viewed smartphone while extending substantially beyond the display footprint into the peripheral retina. Reference radii of 30°–50° were tested to assess sensitivity to this domain choice. Detailed map construction and subtype-sensitivity implementations are provided in Supplementary Methods.

Display geometry and boundary definition

The display was represented as a centered rounded rectangle in visual-angle coordinates. For a point $\boldsymbol{P} = (\boldsymbol{x}, \boldsymbol{y})$, with display half-width a, half-height b, and corner radius r, we defined $\boldsymbol{q_x} = |\boldsymbol{x}| - (\boldsymbol{a} - \boldsymbol{r}), \boldsymbol{q_y} = |\boldsymbol{y}| - (\boldsymbol{b} - \boldsymbol{r})$ (4) and calculated the signed distance to the display boundary as

$$\boldsymbol{d}(\boldsymbol{p}) = \sqrt{\mathbf{max}(\boldsymbol{q_x}, \mathbf{0})^2 + \mathbf{max}(\boldsymbol{q_y}, \mathbf{0})^2} + \mathbf{min}\big(\mathbf{max}(\boldsymbol{q_x}, \boldsymbol{q_y}), \mathbf{0}\big) - \boldsymbol{r}. \quad (5)$$

Negative values of $\boldsymbol{d}(\boldsymbol{p})$ indicate points inside the display, zero denotes the boundary, and positive values indicate points outside the display. The display mask was then defined as $M(p) = \frac{1}{1+\exp[d(p)/\sigma_e]}$, (6) with the boundary-transition scale σ_e fixed at 0.20°. This smooth transition represented the display footprint on the finite visual-field grid, with values approaching 1 within the display and 0 outside it. For regional analyses, the display core was defined by $M(p) \geq 0.9$, and the extra-display surround by $M(p) \leq 0.001$. Intermediate mask values were excluded from regional averaging to minimize numerical contamination of the surround by the display-edge transition. This exclusion affected only the regional averaging domains and did not modify the underlying retinal-stimulus field or represent physical straylight. The primary corner radius was 1.0° and was varied from 0° to 2.0° in sensitivity analyses. Primary analyses assumed centered display alignment.

Pupil and retinal-stimulus scaling

Pupil diameter was estimated using the Watson–Yellott steady-state model [13]. It assumed an age of 25 years, binocular viewing, and an equivalent circular 80° adapting field, corresponding to the modeled 40° visual-field radius. The corresponding adapting-field area was approximately 5,027 square-degrees. Adapting luminance was calculated as the solid-angle-weighted mean of the combined display and surround. The resulting pupil diameters were 4.52, 3.55, and 2.96 mm at surround luminances of 0.01, 10, and 50 cd·m⁻², respectively.

Local α-opic radiance was converted to a pupil-scaled retinal-stimulus estimate using reduced-eye geometry [14] as follows:

$E_{\alpha,j}(x) = L_{\alpha,j}(x)\frac{\pi\,[d_p/2]^2}{f_e^2}$ (7), where d_p is pupil diameter and f_e = 17 mm is the effective focal length of the adult reduced eye. Population-level stimulus from source j was then calculated as $R_{\alpha,j} = \sum_i E_{\alpha,j}\,(i)\,W_{\alpha,i}$, (8) with display and surround contributions retained separately. A fixed 4.52-mm pupil was used as a control to determine whether normalized source-attribution outcomes depended on condition-specific pupil constriction. Because pupil area scales display- and surround-derived stimulus equally within a given condition, it affects absolute retinal-stimulus magnitude but not normalized source attribution.

For physiological comparison, regional retinal illuminance was also expressed in trolands. Photopic retinal illuminance was calculated as $Tv = LvAp$, (9) where $Ap = \pi(dp/2)^2$ (10) is pupil area in mm². Scotopic retinal illuminance was calculated using the corresponding source-specific scotopic-to-photopic ratio. These photopic

and scotopic estimates were calculated from the nominal display and surround luminances without applying the spatial display-mask transition. They were reported as conventional source-specific reference quantities, separately from the retinal-area-weighted regional means used to calculate Δα.

Reference weighting comparisons

To isolate the contribution of receptor topography, source-attribution outcomes were calculated twice under otherwise identical viewing conditions. One calculation used the uniform-density reference, whereas the other used measured rod or cone topography; retinal-area weighting was retained in both cases. A photopic, geometry-only calculation was included as an additional reference. Differences between uniform-density reference and receptor-topography calculations therefore quantify the effect of receptor distribution while holding display geometry, spectral inputs, and pupil scaling constant.

Controlled display and surround analyses

Display luminance, display spectrum, and surround luminance were varied independently to examine their effects on the modeled regional disparity. The controlled grid included D65-like and 5000-K display spectra, display luminances of 10–40 cd·m⁻², and spatially uniform surround luminances of 0.01–10 cd·m⁻². The diffuse-surround intervention held display luminance constant at 40 cd·m⁻². The uniform display-dimming comparison used 40 and 10 cd·m⁻² at a fixed 10 cd·m⁻² surround, whereas the 5000-K versus D65-like comparison used a 40 cd·m⁻² display and a 10 cd·m⁻² surround.

Miller and Kinzey reported low eye-level illuminance during evening smartphone and tablet use in residential bedrooms [15]. To examine a representative low-level diffuse surround independently of those eye-level measurements, we additionally modeled surround luminances of approximately 1.6–3.3 cd·m⁻². For illustrative context, this luminance range would correspond to approximately 10–15 lx incident on Lambertian surfaces with diffuse reflectance of 0.5–0.7. This calculation uses $L = \frac{\rho E}{\pi}$, (11) where L is surface luminance and E is incident illuminance. The absolute change in regional disparity across this range was evaluated relative to the 0.01 cd·m⁻² near-dark viewing.

Dark-mode implementations can differ in luminance distribution and color composition [17,18]. We therefore compared a standardized 25% average picture level (APL) negative-polarity condition with a uniformly dimmed display having the same mean luminance of 10 cd·m⁻². This matched-mean comparison was included as a control to characterize the sensitivity of the region-averaged disparity metric to within-display luminance arrangement. Both matched-mean polarity conditions were evaluated with a 10 cd·m⁻² surround.

Surround spatial heterogeneity was additionally evaluated using 100 panoramas from the photometrically calibrated Laval Indoor HDR dataset [39], derived from the original Laval Indoor HDR dataset [40]. OpenEXR (EXR) pixels were converted to photopic luminance using the dataset calibration, $L = 0.212671R + 0.715160G + 0.072169B$, (12) and reprojected onto a 40° gaze-centered visual field. Four horizontal gaze azimuths (0°, 90°, 180°, and 270°) were evaluated at display luminances of 40 and 10 cd·m⁻². Each HDR surround was compared with a spatially uniform surround matched to its mean extra-display luminance, thereby isolating the effect of spatial luminance distribution. The panoramas retained their calibrated absolute luminance values without tone mapping or scene-wise normalization. The HDR panoramas supplied spatially varying photopic luminance, while receptor-specific calculations used the spatially invariant CIE LED-B3 ambient spectrum rather than deriving pixel-specific spectra from the HDR RGB values.

Outcomes

The principal source-attribution outcomes were display-population overlap and display-source fraction. Display-population overlap was defined as the fraction of the modeled receptor population assigned to the display by the continuous display mask. For receptor channel α, it was calculated as $P_{\alpha,\,\mathrm{disp}} = \sum_i M_i D_{\alpha,i} A_i / \sum_i D_{\alpha,i} A_i$ (13), where M_i is the display-mask value, $D_{\alpha,i}$ is receptor-density weighting, and A_i is represented retinal area. The display-overlap ratio was defined as the receptor-specific display-population overlap divided by the corresponding uniform-density retinal-area overlap. Values below 1 therefore indicate relative depletion within the display footprint, whereas values above 1 indicate relative enrichment. For receptor channel α, the display-source fraction was defined as $F_{disp,\alpha} = \frac{R_{\alpha,disp}}{R_{\alpha,disp} + R_{\alpha,surround}}$, (14) where $R_{\alpha,disp}$ and $R_{\alpha,surround}$ are the integrated display- and surround-derived contributions, respectively.

Crossover luminance was retained as a secondary descriptive index and defined as the surround luminance at which the two integrated contributions were equal. It is a model-defined, domain-dependent descriptive index rather than a physiological threshold.

For each selected region (display core or extra-display surround), the mean α-opic retinal stimulus was calculated using retinal-area weighting alone:

$\bar{E}_{\alpha,\mathcal{R}} = \frac{\sum_{i \in \mathcal{R}} A_i E_{\alpha,i}}{\sum_{i \in \mathcal{R}} A_i}$ (15).

Here, $E_{\alpha,i}$ denotes the local α-opic retinal stimulus, A_i the represented retinal area, and $\mathcal{R}$ the selected region. Regional disparity was defined as $\Delta\alpha = \log_{10}\left(\frac{\bar{E}_{\alpha,core}}{\bar{E}_{\alpha,surround}}\right)$, (16) where $\bar{E}_{\alpha,core}$ and $\bar{E}_{\alpha,surround}$ are the retinal-area-weighted mean α-opic retinal-stimulus values within the display core and extra-display surround, respectively. These regional means were calculated using a common spatial domain and retinal-area weighting across all receptor channels, without receptor-density weighting. Thus, regional disparity is independent of receptor topography, which instead enters through display-population overlap and the population-integrated display-source fraction. For the controlled lighting analyses, the reduction in regional disparity was calculated relative to the 0.01 cd·m⁻² near-dark reference at the same display luminance and spectral composition:

$\Delta\Delta_\alpha = \Delta_{\alpha,\,\text{near-dark}} - \Delta_{\alpha,\,\text{condition}}$, (17) in $\log_{10}$ units. Separately, photopic and scotopic retinal illuminances were estimated from source luminance and pupil area for physiological context.

Sensitivity analyses and numerical verification

Sensitivity analyses assessed dependence on spectral inputs, receptor anatomy, viewing geometry, and numerical settings. Display and ambient spectra, analysis radius, display corner radius, and grid spacing were varied according to prespecified sensitivity analyses. Anatomical sensitivity analyses included constrained variation in rod and total-cone distributions, together with the S-cone and L/M cases described under Receptor topography and retinal coordinates.

A 300-case Latin hypercube analysis jointly varied display luminance, near-dark surround luminance, and viewing distance across the prespecified ranges in Supplementary Table S1. Numerical verification included checks of input integrity, finite outputs, implementation consistency, and grid convergence.

Use of large language models

ChatGPT (OpenAI) was used during manuscript preparation for language refinement, structural editing, and code-assisted verification. All scientific decisions, model design, analyses, interpretation, and final manuscript content were reviewed and approved by the authors. The authors take full responsibility for the content of the work.

Data availability

No new experimental or participant-level data were generated in this study. All anatomical, spectral, colorimetric, and HDR input data were obtained from previously published sources cited in the manuscript. Third-party datasets are not redistributed as part of this study and should be obtained directly from their original providers under the applicable access conditions. The model-generated numerical results and reproducibility documentation will be made publicly available alongside the authors' original computational code.

Code and model availability

The custom Python code developed for this study, including the computational model, analysis scripts, and reproducibility documentation, is available to editors and reviewers during peer review through a private Zenodo preview link provided confidentially to the editorial office. The publication-associated version will be released through a public GitHub repository and permanently archived on Zenodo with a version-specific DOI. Third-party input datasets are not redistributed and must be obtained from their original sources, as documented in the repository.

References

1. Curcio, C. A., Sloan, K. R., Kalina, R. E. & Hendrickson, A. E. Human photoreceptor topography. *J. Comp. Neurol.* **292,** 497–523 (1990). doi:10.1002/cne.902920402.
2. Drasdo, N. & Fowler, C. W. Non-linear projection of the retinal image in a wide-angle schematic eye. *Br. J. Ophthalmol.* **58,** 709–714 (1974). doi:10.1136/bjo.58.8.709.
3. Antona, B. et al. Symptoms associated with reading from a smartphone in conditions of light and dark. *Appl. Ergon.* **68,** 12–17 (2018). doi:10.1016/j.apergo.2017.10.014.
4. Mehravin, M. et al. The effect of ambient light intensity on transient changes in refraction and ocular biometric components following near work: a randomized clinical trial. *J. Curr. Ophthalmol.* **37,** 115–123 (2025). doi:10.4103/joco.joco_149_25.
5. Oh, J. H., Yoo, H., Park, H. K. & Do, Y. R. Analysis of circadian properties and healthy levels of blue light from smartphones at night. *Sci. Rep.* **5,** 11325 (2015). doi:10.1038/srep11325.
6. Xu, W. et al. Ambient lighting strategy of visual display terminals in micro-space luminous environment under low-light conditions. *Build. Environ.* **276,** 112859 (2025). doi:10.1016/j.buildenv.2025.112859.
7. Wang, B. et al. Effect of indoor ambient luminance distribution on smartphone display luminance and occupant visual comfort through visual field luminance sensitivity model. *Build. Environ.* **288,** 113919 (2026). doi:10.1016/j.buildenv.2025.113919.
8. Chu, Y. et al. A visual field light distribution model for enhanced visual comfort. *Build. Environ.* **304,** 115072 (2026). doi:10.1016/j.buildenv.2026.115072.
9. Chawla, A. S. & Samei, E. Ambient illumination revisited: a new adaptation-based approach for optimizing medical imaging reading environments. *Med. Phys.* **34,** 81–90 (2007). doi:10.1118/1.2402583.

10. Gloriani, A. H. et al. Influence of background size, luminance and eccentricity on different adaptation mechanisms. *Vision Res.* **125,** 12–22 (2016). doi:10.1016/j.visres.2016.04.008.
11. Sonntag, A. et al. Effect of central and peripheral cone- and rod-specific stimulation on the pupillary light reflex. *Int. Ophthalmol.* **42,** 1427–1436 (2022). doi:10.1007/s10792-021-02132-1.
12. CIE. CIE S 026/E:2018 CIE System for Metrology of Optical Radiation for ipRGC-Influenced Responses to Light. (CIE, 2018). doi:10.25039/S026.2018.
13. Watson, A. B. & Yellott, J. I. A unified formula for light-adapted pupil size. *J. Vis.* **12,** 12 (2012). doi:10.1167/12.10.12.
14. International Commission on Non-Ionizing Radiation Protection (ICNIRP). ICNIRP guidelines on limits of exposure to incoherent visible and infrared radiation. *Health Phys.* **105,** 74–96 (2013). doi:10.1097/HP.0b013e318289a611.
15. Miller, N. J. & Kinzey, B. R. Home nighttime light exposures: How much are we really getting in our residences? *Lighting Design + Application*. **48**, 48–54 (2018). https://doi.org/10.1177/036063251804800715.
16. Na, N. & Suk, H.-J. Adaptive display luminance for viewing smartphones under low illuminance. *Opt. Express.* **23,** 16912–16920 (2015). doi:10.1364/OE.23.016912.
17. Dash, P. & Hu, Y. C. How much battery does dark mode save?: an accurate OLED display power profiler for modern smartphones. *in Proceedings of the 19th Annual International Conference on Mobile Systems, Applications, and Services* 323–335 (ACM, 2021). doi:10.1145/3458864.3467682.
18. Xie, X., Song, F., Liu, Y., Wang, S. & Yu, D. Study on the effects of display color mode and luminance contrast on visual fatigue. *IEEE Access.* **9,** 35915–35923 (2021). doi:10.1109/ACCESS.2021.3061770.
19. Shi, Y. et al. Spectral influence of the normal LCD, blue-shifted LCD, and OLED smartphone displays on visual fatigue: a comparative study. *Displays.* **69,** 102066 (2021). doi:10.1016/j.displa.2021.102066.
20. Ide, T., Toda, I., Miki, E. & Tsubota, K. Effect of blue light-reducing eye glasses on critical flicker frequency. *Asia-Pac. J. Ophthalmol.* **4,** 80–85 (2015). doi:10.1097/APO.0000000000000069.
21. Lin, J. B., Gerratt, B. W., Bassi, C. J. & Apte, R. S. Short-wavelength light-blocking eyeglasses attenuate symptoms of eye fatigue. *Invest. Ophthalmol. Vis. Sci.* **58,** 442–447 (2017). doi:10.1167/iovs.16-20663.
22. Rosenfield, M., Li, R. T. & Kirsch, N. T. A double-blind test of blue-blocking filters on symptoms of digital eye strain. *Work.* **65,** 343–348 (2020). doi:10.3233/WOR-203086.
23. Singh, S., Downie, L. E. & Anderson, A. J. Do blue-blocking lenses reduce eye strain from extended screen time? A double-masked randomized controlled trial. *Am. J. Ophthalmol.* **226,** 243–251 (2021). doi:10.1016/j.ajo.2021.02.010.
24. Vera, J. et al. Blue-blocking filters do not alleviate signs and symptoms of digital eye strain. *Clin. Exp. Optom.* **106,** 85–90 (2023). doi:10.1080/08164622.2021.2018914.
25. Hastings, G. D., Tiruveedhula, P. & Roorda, A. Wide-field optical eye models for emmetropic and myopic eyes. *J. Vis.* **24,** 9 (2024). doi:10.1167/jov.24.7.9.
26. Smith, E. L. III, Hung, L.-F. & Huang, J. Relative peripheral hyperopic defocus alters central refractive development in infant monkeys. *Vision Res.* **49,** 2386–2392 (2009). doi:10.1016/j.visres.2009.07.011.
27. Berntsen, D. A., Barr, C. D., Mutti, D. O. & Zadnik, K. Peripheral defocus and myopia progression in myopic children randomly assigned to wear single vision and progressive addition lenses. *Invest. Ophthalmol. Vis. Sci.* **54,** 5761–5770 (2013). doi:10.1167/iovs.13-11904.
28. Atchison, D. A. et al. Relative peripheral hyperopia does not predict development and progression of myopia in children. *Invest. Ophthalmol. Vis. Sci.* **56,** 6162–6170 (2015). doi:10.1167/iovs.15-17200.
29. Ciuffreda, K. J. & Vasudevan, B. Nearwork-induced transient myopia (NITM) and permanent myopia—is there a link? *Ophthalmic Physiol. Opt.* **28,** 103–114 (2008). doi:10.1111/j.1475-1313.2008.00550.x.
30. Curcio, C. A. et al. Distribution and morphology of human cone photoreceptors stained with anti-blue opsin. *J. Comp. Neurol.* **312,** 610–624 (1991). doi:10.1002/cne.903120411.

31. Ahnelt, P. K., Kolb, H. & Pflug, R. Identification of a subtype of cone photoreceptor, likely to be blue sensitive, in the human retina. *J. Comp. Neurol.* **255,** 18–34 (1987). doi:10.1002/cne.902550103.
32. Kuchenbecker, J. A., Sahay, M., Tait, D. M., Neitz, M. & Neitz, J. Topography of the long- to middle-wavelength sensitive cone ratio in the human retina assessed with a wide-field color multifocal electroretinogram. *Vis. Neurosci.* **25,** 301–306 (2008). doi:10.1017/S0952523808080474.
33. Samsung Electronics. Beautifully crafted from metal and glass, Samsung Galaxy S6 and Galaxy S6 edge define what's next in mobility. *Samsung Global Newsroom* https://news.samsung.com/global/beautifully-crafted-from-metal-and-glass-samsung-galaxy-s6-and-galaxy-s6-edge-define-whats-next-in-mobility (2015).
34. Yeo, H.-S., Lee, J., Bianchi, A., Harris-Birtill, D. & Quigley, A. SpeCam: sensing surface color and material with the front-facing camera of a mobile device. in Proceedings of the 19th International Conference on Human-Computer Interaction with Mobile Devices and Services Article 25, 1–9 (ACM, New York, 2017). doi:10.1145/3098279.3098541.
35. Vos, J. J. & van den Berg, T. J. T. P. Report on disability glare. CIE 135/1-1999 (CIE, 1999).
36. CIE TC 1-85. CIE 015:2018 Colorimetry, 4th Edition. (CIE, 2018). doi:10.25039/TR.015.2018.
37. CIE. CIE 1931 colour-matching functions, 2 degree observer. (2019). doi:10.25039/CIE.DS.xvudnb9b.
38. Quigley, H. A., Brown, A. E., Morrison, J. D. & Drance, S. M. The size and shape of the optic disc in normal human eyes. *Arch. Ophthalmol.* **108,** 51–57 (1990). doi:10.1001/archopht.1990.01070030057028.
39. Bolduc, C., Giroux, J., Hébert, M., Demers, C. & Lalonde, J.-F. Beyond the pixel: a photometrically calibrated HDR dataset for luminance and color prediction. *in Proceedings of the IEEE/CVF International Conference on Computer Vision (ICCV)* 8071–8081 (2023). doi:10.1109/ICCV51070.2023.00741.
40. Gardner, M.-A. et al. Learning to predict indoor illumination from a single image. *ACM Trans. Graph.* **36,** 176 (2017). doi:10.1145/3130800.3130891.

Author contributions

S.Z. conceived and designed the study, developed the computational framework, curated and processed the input data, implemented the model and analyses, performed validation and sensitivity analyses, prepared the figures and tables, and wrote the original manuscript. S.-W.L. supervised the study and critically reviewed and edited the manuscript. Both authors reviewed and approved the final manuscript.

Funding

The authors received no specific funding for this work.

Competing interests

The authors declare no competing interests.